Available online at www.sciencedirect.com
SCIENCE DIRECT
International Journal of Thermal Sciences 45 (2006) 1008–1020
International Journal of Thermal Sciences
www.elsevier.com/locate/ijts

Fluid flow and convective heat transfer in a rotating helical square duct

Yitung Chen [a,*], Huajun Chen [a,b], Benzhao Zhang [b], Hsuan-Tsung Hsieh [a]

[a] *Department of Mechanical Engineering, University of Nevada, Las Vegas, NV89154, USA*
[b] *Department of mechanics, Zhejiang University, Hangzhou, 310027, PR China*

Received 27 December 2004; received in revised form 1 November 2005; accepted 13 January 2006

Available online 28 February 2006

Abstract

A numerical study is performed to examine the characteristics of fluid flow and convective heat transfer in a helical square duct rotating at a constant angular velocity about the center of curvature. Due to the combined effects of rotation (the Coriolis force), torsion and curvature (the centrifugal force), the flow behaviors become very complicated. A wide range of parameters is covered in this work. The variations of flow structure and temperature distribution with the force ratio F (the ratio of the Coriolis force to the centrifugal force) and the torsion are examined in details. The effects of rotation and torsion on the friction factor and Nusselt number are also studied at length. And also multiple solutions for a rotating toroidal square duct have been obtained. Certain hitherto unknown flow patterns are found. The present work shows both the nature of flow behaviors and the characteristics of heat transfer in a rotating helical square duct.

Keywords: Secondary flow; Heat transfer; Rotating duct; Helical duct

1. Introduction

The flow of a fluid through a non-straight pipe system creates a secondary flow taking place in a plane perpendicular to the main flow. Although the magnitude of the secondary flow is much smaller than the main flow, it has been verified that the secondary flow can enhance the heat transfer significantly in cooled ducts. Additionally, a higher secondary flow produces a higher flow resistance, which results in the main flow requiring more power to sustain the axial flux as compared to flows in a straight pipe/duct without secondary flow. On the other hand, secondary flows lead to vibrations and noises. Because secondary flow is one of the most important aspects of flow dynamics in non-straight pipe systems, knowledge and understanding of flow physics are important in engineering designs and operations.

Because of the importance of secondary flow in engineering applications, the characteristics of the complex hydrodynamic phenomenon have been the subject of many studies. Secondary flows in stationary curved ducts (with or without finite pitches) related to engineering applications for different cross-sections have been investigated theoretically, numerically and experimentally. Berger et al. [1], Nandakumar and Masliyah [2], Ito [3] and Berger [4] have reviewed fluid flow and heat transfer in curved ducts.

To enhance the rate of heat and mass transfer, the helical ducts with a finite pitch have been used extensively in various industrial applications. Useful characteristics include high rates of heat and mass transfer, enhanced cross-sectional mixing, low axial dispersion and an extended laminar flow. Previous work by Germano [5], Tuttle [6], Liu and Masliyah [7], Zabielski and Mestel [8] on helical ducts were mainly focused on stationary ducts with a circular cross sections. Only a few studies took helical square ducts into account. Chen and Jan [9] studied the torsion effect on fully developed laminar flow in helical square ducts with the Galerkin finite-element method and found that the Dean instability can be avoided due to the torsion. On the other hand Boliander [10,11] obtained the opposite conclusion when he studied the helical square ducts with a finite volume method and detected two unconditionally stable solution branches. Thomson et al. [12] examined the convective heat transfer in helical ducts with a rectangular cross section in

* Corresponding author. Tel.: +(702)895 1202; fax: +(702)895 3936.
E-mail address: uuchen@nscee.edu (Y. Chen).

1290-0729/$ – see front matter
doi:10.1016/j.ijthermalsci.2006.01.006

Nomenclature

a	width of the helical square duct ..... m
$\mathbf{a}_c, \mathbf{a}_e$	Coriolis acceleration and relative acceleration of the flow ..... $\mathrm{m\,s^{-2}}$
c_p	heat capacity at constant pressure .... $\mathrm{J\,kg^{-1}\,K^{-1}}$
d_H	hydrodynamic diameter, $d_H = a$ ..... m
Dn	Dean number, $= Re\,\kappa^{1/2}$
f, Nu	friction factor and Nusselt number of a rotating helical square duct
f_s, Nu_s	friction factor and Nusselt number for a stationary straight duct
F	ratio of the Coriolis force to the centrifugal force, $= \Omega R\cos\beta/w_m$
$\mathbf{g_1}, \mathbf{g_2}, \mathbf{g_3}$	natural base vectors of the helical coordinate system (x, y, s)
$\mathbf{g_{ij}}$	metric tensors
g	gravitational accelerate ..... $\mathrm{m\,s^{-2}}$
Gr	Grashof number, $= \frac{g\chi\Delta T d_H^3}{\nu^2}$
K	pitch of the helix ..... m
p^*	pressure ..... Pa
Pr	Prandtl number, $= \frac{\nu}{\alpha}$
q_w	wall heat flux ..... $\mathrm{W\,m^{-2}\,K^{-1}}$
R	curvature radius ..... m
Re	Reynolds number, $= w_m d_H/\nu$
s^*	axial direction coordinate ..... m
$(\mathbf{T}, \mathbf{N}, \mathbf{B})$	unit tangent, normal and binormal vectors of the centerline of the duct
T^*, T_w^*	temperature of fluid and wall ..... (°C, K)
T_b^*	bulk mean temperature ..... (°C, K)
u^*, v^*, w^*	physical velocity components in x, y and s directions ..... $\mathrm{m\,s^{-1}}$
U	characteristic velocity ..... $\mathrm{m\,s^{-1}}$
w_m^*	mean axial velocity ..... $\mathrm{m\,s^{-1}}$
(x^*, y^*, s^*)	helical coordinate system ..... m

Greek symbols

α	thermal diffusivity ..... $\mathrm{m^2\,s^{-1}}$
β	slope between the helix and the horizontal plane
ν	kinematic viscosity of fluid ..... $\mathrm{m\,s^{-2}}$
ρ	density of the fluid ..... $\mathrm{kg\,m^{-3}}$
Γ_{ij}^k	Christoffel symbols
κ^*	curvature ..... $\mathrm{m^{-1}}$
τ^*	torsion ..... $\mathrm{m^{-1}}$
Ω^*	rotating angular velocity
ψ	stream function
ΔT	representative temperature difference, $Pr\,d_H\,\partial T/\partial s$ ..... (°C, K)
χ	thermal expansion coefficient ..... $\mathrm{K^{-1}}$

Subscript and superscript

$*$	dimensional variable
max	maximum value

low Dean numbers and found that torsion could be minimized to enhance heat transfer.

When a duct rotates about an axis normal to a plane including the duct, the Coriolis force can also contribute to the generation of secondary flow. Such rotating ducts have extensive applications, such as the cooling systems for conductors of electric generator motors, gas turbines, and separation processes. As an interesting problem, the combined effects of curvature and rotation, which are relevant to the flow in rotating curved ducts, have been examined in details by numerous researchers. Ludwieg [13] first analyzed the flow in a rotating toroidal rectangular duct theoretically and developed a solution based on the integral method. Miyazaki studied the characteristics of the flow and heat transfer dynamics in the boundary layer of rotating toroidally curved circular [14] and rectangular [15] ducts using finite-difference method and predicted an increase of the friction factor with an increase in the strength of rotation. However, their work was only for the co-rotating cases (the rotating angular velocity and the axial velocity are in the same direction).

Ito and Motai [16] first studied the fluid flow in both co-rotating and counter-rotating (the rotating angular velocity and the axial velocity are in the opposites directions) curved ducts theoretically. They predicted a reduction in the strength and a reversal in the direction of the secondary flow for a small parameter. Menon [17] confirmed the reversal of the secondary flow even for high Dean numbers. Ito et al. [18] studied the friction factor in a rotating toroidally curved pipe numerically and experimentally for the cases of a constant Dean number but their computations were limited to relatively small parameters. Ishigaki [19] examined the flow characteristics and friction factor numerically for both counter-rotating and co-rotating curved pipes with a small curvature and a circular cross-section. He introduced a new parameter F, which represents the ratio of the Coriolis force to the centrifugal force and studied the flow transitions as a function of F for two Dean numbers. Wang and Cheng [20] conducted a detailed study of the flow structure in a rotating toroidal square duct when the wall was heated and cooled. Yamamoto et al. [21] employed the spectral method to examine the flow structure and the flow rate in a rotating curved square duct. They found that the maximum number of secondary cells to be six. But in the same paper, they predicted that there should be more complex cell structures, which they did not obtain. Zhang et al. [22] studied the flow structure and friction factor in a rotating rectangular duct for a wide range of rotational speeds and found more complex cell structures. Zhang et al. [23] employed the perturbation method study the flow in a toroidal annular pipe. Their work was focused on the effect on the inner wall of the pipe and revealed an eight-cell structure of the secondary flow when the centrifugal force balanced the Coriolis force. All these results indicate that the secondary flow in rotating curved pipes is more complex than

that found in stationary curved pipes. The results for flows and heat transfer in stationary pipes are not suitable for extrapolation to rotating pipes.

Because the characteristics of fluid flow and heat transfer in rotating helical square ducts are not well understood and there is no literature regarding the flow and heat transfer in rotating helical ducts with a square cross section, it is quite necessary and useful to investigate this problem. The primary objective of this paper is to examine the effects of rotation and torsion on flow structure and convective heat transfer. We also present a relatively comprehensive numerical analysis of the effects of rotation and torsion on flow behaviors, temperature distributions, friction factors and Nusselt numbers. Additionally, the bifurcation phenomena in the rotating toroidal ducts have also been revealed. The present study provides some useful information on the design of such pipe flow systems.

2. Governing equations

Fig. 1 shows a helical square duct rotating around the axis OZ^* with a constant angular velocity Ω^*. The centerline of the helical duct is described by the position vector $\mathbf{r}^*_{\mathbf{o}'}$; s is along the axial direction of the helical square duct. R is the curvature radius and $2\pi K$ is the pitch. The width of the helical square duct is a. Along the centerline, the unit tangent, the normal vector and binormal vector are mutually orthogonal and are denoted as $\mathbf{T}$, $\mathbf{N}$ and $\mathbf{B}$, respectively. In the helical coordinate system (x^*, y^*, s^*), x^*, y^* are defined by the plane of $(\mathbf{N}, \mathbf{B})$ and the position vector at an arbitrary point c can be expressed as follows:

$$\mathbf{r}^*_{\mathbf{c}} = \mathbf{r}^*_{\mathbf{o}'}(s) + x^*\mathbf{N} + y^*\mathbf{B} \tag{1}$$

The natural base vectors of the helical coordinate system (x^*, y^*, s^*) are given by

$$\mathbf{g_1} = \partial \mathbf{r}^*_{\mathbf{c}}/\partial x^* = \mathbf{N}$$
$$\mathbf{g_2} = \partial \mathbf{r}^*_{\mathbf{c}}/\partial y^* = \mathbf{B}$$
$$\mathbf{g_3} = \partial \mathbf{r}^*_{\mathbf{c}}/\partial s^* = M\mathbf{T} - \tau^* y^*\mathbf{N} + \tau^* x^*\mathbf{B} \tag{2}$$

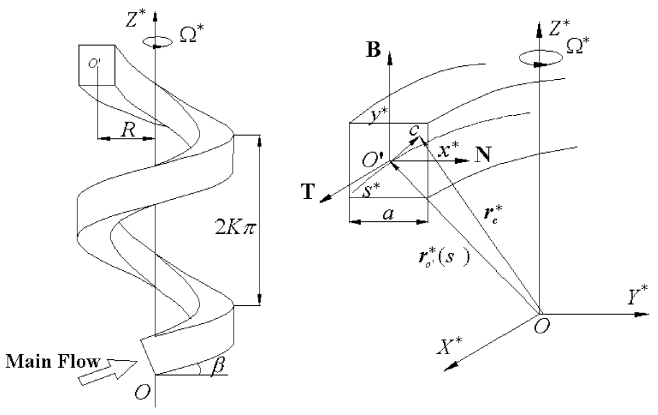

Fig. 1. Rotating helical square duct and the coordinate system.

where $M = 1 - \kappa^* x$, κ^* is the curvature and τ^* is the torsion, which are defined as:

$$\kappa^* = \frac{R}{R^2 + K^2}, \qquad \tau^* = \frac{K}{R^2 + K^2} \tag{3}$$

However, the natural basis $(\mathbf{g_1}, \mathbf{g_2}, \mathbf{g_3})$ are non-orthogonal. It is more convenient to expand the velocity in the physical basis $(\mathbf{N}, \mathbf{B}, \mathbf{T})$. So the metric tensors are

$$[\mathbf{g_{ij}}] = \begin{bmatrix} 1 & 0 & -\tau^* y^* \\ 0 & 1 & \tau^* x^* \\ -\tau^* y^* & \tau^* x^* & M^2 + \tau^{*2} y^{*2} + \tau^{*2} x^{*2} \end{bmatrix} \tag{4}$$

and non-zero Christoffel symbols are

$$\Gamma^1_{13} = \Gamma^1_{31} = -\frac{\kappa^* \tau^* y^*}{M}$$
$$\Gamma^1_{23} = \Gamma^1_{32} = -\tau^*$$
$$\Gamma^1_{33} = \kappa^* M - \tau^{*2} x^* + \frac{\kappa^* \tau^{*2} y^{*2}}{M}$$
$$\Gamma^2_{13} = \Gamma^2_{31} = \frac{\tau^*}{M}$$
$$\Gamma^2_{33} = -\frac{\tau^{*2} y^*}{M}$$
$$\Gamma^3_{13} = \Gamma^3_{31} = -\frac{\kappa^*}{M}$$
$$\Gamma^2_{33} = \frac{\kappa^* \tau^* y^*}{M} \tag{5}$$

The velocity in the physical basis can be expressed as

$$\mathbf{V} = u^*\mathbf{N} + v^*\mathbf{B} + w^*\mathbf{T} \tag{6}$$

where u^*, v^* and w^* are the velocity components in the directions $\mathbf{N}$, $\mathbf{B}$, and $\mathbf{T}$, respectively.

The Coriolis acceleration $\mathbf{a_c}$ and the relative acceleration $\mathbf{a_e}$ can be obtained as

$$\mathbf{a_c} = (2\Omega^* w^* \cos\beta - 2\Omega^* v^* \sin\beta)\mathbf{N} - 2\Omega^* u^* \cos\beta\mathbf{T} + 2\Omega^* u^* \sin\beta\mathbf{B} \tag{7}$$

$$\mathbf{a_e} = \Omega^{*2}(R - x^*)\mathbf{N} + \frac{1}{2}\Omega^{*2} y^* \sin 2\beta\mathbf{T} - \Omega^{*2} y^* \sin^2\beta\mathbf{B} \tag{8}$$

where β is the slope between the centerline of the duct and the horizontal plane.

It is assumed that the fluid flow is steady, laminar and fully developed. The thermal condition on the pipe wall is axially uniform heat flux q_w with peripherally uniform wall temperature T_w [20]. Heat conduction in the direction of the duct axis is neglected. The importance of buoyancy forces in a mixed convection flow can be measured by the ratio of Grashof and Reynolds numbers:

$$\frac{Gr}{Re^2} = \frac{g\chi\Delta T d_H}{w^{*2}_m} \tag{9}$$

where g is the gravity accelerate, w^*_m is the mean axial velocity, χ is the thermal expansion coefficient, ΔT is the temperature difference, and d_H is the dynamic diameter and here $d_H = a$. When this number approaches or exceeds unity, the buoyancy contributions to the flow will be strong. Conversely, if it is very small, buoyancy forces can be ignored. In this paper, we only

consider the cases that $\frac{Gr}{Re^2} \ll 1$. Hence, the buoyancy force due to fluid density variation is very weak comparing the magnitude order of centrifugal force and Coriolis force and is neglected in this work

The following dimensionless parameters are introduced:

$$(x, y, s) = \frac{(x^*, y^*, s^*)}{d_H}, \qquad (u, v) = \frac{(u^*, v^*)d_H}{\nu}$$

$$w = \frac{w^*}{w_m^*}, \qquad P = \frac{P^* d_H^2}{\rho \nu^2}$$

$$T = \frac{(T_w^* - T^*)}{\Delta T}, \qquad \kappa = \kappa^* d_H, \qquad \tau = \tau^* d_H$$

$$\Omega = \frac{\Omega^* d_H^{*2}}{\nu}, \qquad Pr = \frac{\nu}{\alpha}$$

where, ρ is the fluid density, ν is the kinematic viscosity, α is the thermal diffusivity of the fluid, ΔT is defined as $Pr\, d_H \frac{\partial T}{\partial s}$, here Pr is the Prandtl number. In terms of tensor analysis, we can obtain the continuity, Navier–Stokes and energy equations as

$$\frac{\partial}{\partial x}(Mu + Gnyw) + \frac{\partial}{\partial y}(Mv - Gnxw) = 0 \tag{10}$$

$$\left(u + Gn\frac{y}{M}w\right)\frac{\partial u}{\partial x} + \left(v - Gn\frac{x}{M}w\right)\frac{\partial u}{\partial y} + \frac{w}{M}\left(Dn^2 w - Gnv\right) = -\frac{\partial P}{\partial x} - 2F\left(Dn^2 w - Gnv\right) + \left(\nabla^2 \mathbf{V}\right)^{(1)} \tag{11}$$

$$\left(u + Gn\frac{y}{M}w\right)\frac{\partial v}{\partial x} + \left(v - Gn\frac{x}{M}w\right)\frac{\partial v}{\partial y} + Gn\frac{wu}{M} = -\frac{\partial P}{\partial y} - 2FGnu + \left(\nabla^2 \mathbf{V}\right)^{(2)} \tag{12}$$

$$\left(u + Gn\frac{y}{M}w\right)\frac{\partial w}{\partial x} + \left(v - Gn\frac{x}{M}w\right)\frac{\partial w}{\partial y} - \frac{\kappa}{M}wu = -\frac{\sqrt{\kappa}}{M\,Dn}\left(\frac{\partial P}{\partial s} + \tau y\frac{\partial P}{\partial x} - \tau x\frac{\partial P}{\partial y}\right) + 2F\kappa u + \left(\nabla^2 \mathbf{V}\right)^{(3)} \tag{13}$$

$$Pr\left(\left(u + Gn\frac{y}{M}w\right)\frac{\partial T}{\partial x} + \left(v - Gn\frac{x}{M}w\right)\frac{\partial T}{\partial y}\right) - \frac{Dn}{M\sqrt{\kappa}}w = \left(\nabla^2 T\right) \tag{14}$$

where

$$\left(\nabla^2 \mathbf{V}\right)^{(1)} = \frac{1}{M^2}\Big[\left(M^2 + \tau^2 y^2\right)\frac{\partial^2 u}{\partial^2 x} + \left(M^2 + \tau^2 x^2\right)\frac{\partial^2 u}{\partial^2 y} - 2\tau^2 xy\frac{\partial^2 u}{\partial x\,\partial y} + A\frac{\partial u}{\partial x} - B\frac{\partial u}{\partial y} - 2\tau^2 y\frac{\partial v}{\partial x} + 2\tau^2 x\frac{\partial u}{\partial y} + 2\kappa\tau y\frac{\partial w}{\partial x} - 2\kappa\tau x\frac{\partial w}{\partial y} - \left(\kappa^2 + \tau^2\right)u - Cv + Dw\Big]$$

$$\left(\nabla^2 \mathbf{V}\right)^{(2)} = \frac{1}{M^2}\Big[\left(M^2 + \tau^2 y^2\right)\frac{\partial^2 v}{\partial^2 x} + \left(M^2 + \tau^2 x^2\right)\frac{\partial^2 v}{\partial^2 y} - 2\tau^2 xy\frac{\partial^2 v}{\partial x\,\partial y} + A\frac{\partial v}{\partial x} - B\frac{\partial v}{\partial y} + 2\tau^2 y\frac{\partial u}{\partial x} - 2\tau^2 x\frac{\partial u}{\partial y} + 2\kappa\tau y\frac{\partial w}{\partial x} - 2\kappa\tau x\frac{\partial w}{\partial y} - Cu - \tau^2 v + \kappa\tau w\Big]$$

$$\left(\nabla^2 \mathbf{V}\right)^{(3)} = \frac{1}{M^2}\Big[\left(M^2 + \tau^2 y^2\right)\frac{\partial^2 w}{\partial^2 x} + \left(M^2 + \tau^2 x^2\right)\frac{\partial^2 w}{\partial^2 y} - 2\tau^2 xy\frac{\partial^2 w}{\partial x\,\partial y} + A\frac{\partial w}{\partial x} - B\frac{\partial w}{\partial y} - 2\kappa\tau y\frac{\partial u}{\partial x} + 2\kappa\tau x\frac{\partial u}{\partial y} - Du + \kappa\tau v - \kappa^2 w\Big]$$

$$\left(\nabla^2 T\right) = \frac{1}{M^2}\Big[\left(M^2 + \tau^2 y^2\right)\frac{\partial^2 T}{\partial^2 x} + \left(M^2 + \tau^2 x^2\right)\frac{\partial^2 T}{\partial^2 y} - 2\tau^2 xy\frac{\partial^2 T}{\partial x\,\partial y} + A\frac{\partial T}{\partial x} - B\frac{\partial T}{\partial y}\Big]$$

$$A = \frac{\kappa\tau^2 y^2}{M} - \tau^2 x - \kappa M, \qquad B = \frac{\tau^2 y}{M}$$

$$C = \frac{\kappa\tau^2 y}{M}, \qquad D = \frac{\kappa^2 \tau y}{M}$$

$$M = 1 - \kappa x, \qquad Gn = \tau\, Re \quad \text{and}$$

$$P = p - \frac{1}{2\kappa^2}\Omega^2(1 - \kappa x)^2 - \frac{1}{2}\Omega^2 y^2 \sin^2\beta$$

In the above equations, it can be easily concluded that the flow and heat transfer in a rotating helical pipe with a square cross-section are affected by the following parameters:

The curvature κ: representing the ratio of the centrifugal force to the inertial force.

The torsion τ: representing the twist force to the inertial force.

The Dean number Dn: $Dn = Re\sqrt{\kappa}$ ($Re = w_m^* d_H/\nu$), a square root of the product of (inertial force/viscous force) and (centrifugal force/viscous force).

The F number: $F = \Omega^* R\cos\beta/w_m^*$, representing the ratio of the Coriolis force to centrifugal force. $F > 0$ means a co-rotation case, $F < 0$ means a counter-rotation case, $F = 0$ means a stationary case.

The Prandtl number Pr: $Pr = \nu/\alpha$, is a thermophysical property parameter, representing the ratio of momentum diffusion rate to the thermal diffusion rate.

The stream function ψ, which automatically satisfies the continuity equation, may be defined according to

$$\frac{\partial \psi}{\partial y} = Mu + Gnyw, \qquad -\frac{\partial \psi}{\partial x} = Mv - Gnxw \tag{15}$$

Substituting Eqs. (15) into the energy equation (14), we can obtain

$$\frac{Pr}{M}\left(\frac{\partial \psi}{\partial y}\frac{\partial T}{\partial x} - \frac{\partial \psi}{\partial x}\frac{\partial T}{\partial y}\right) - \frac{Dn}{M\sqrt{\kappa}}w = \left(\nabla^2 T\right) \tag{16}$$

From Eq. (16), we found that the axial convection of the main flow is divided into two parts: one part is absorbed into the stream function, combining the effects of τ and Pr, and the another part is independent of Pr. When Pr is very small, the heat convection can be neglected and the energy equation can be expressed as

$$-\frac{Dn}{M\sqrt{\kappa}}w = \left(\nabla^2 T\right) \tag{17}$$

Eq. (17) is the heat conduction equation with a heat source, which is similar to the convection equation in stationary straight pips with no body force. When Pr is nearly equal to 1, the energy equation (17) will show similarity with axial momentum equation (13) for a small F. The temperature distribution for this condition will be similar to the axial velocity distribution. When Pr is very large, the axial convection can be ignored and the energy equation (16) can be expressed as

$$\frac{Pr}{M}\left(\frac{\partial\psi}{\partial y}\frac{\partial T}{\partial x} - \frac{\partial\psi}{\partial x}\frac{\partial T}{\partial y}\right) = \left(\nabla^2 T\right) \tag{18}$$

From this equation, we can find that the distribution of the streamline decides the heat transfer characteristics. In this case, the isothermal lines outside the thermal boundary layer are strongly correlated with the streamline of the secondary flow. In this paper, the Prandtl number will be confined to the case of $Pr = 0.71$, which means the distribution of temperature is similar to that of the axial velocity.

The boundary conditions are

$$\text{At } x = \pm 1/2 \text{ and } y = \pm 1/2, \quad u = v = w = T = \psi = 0 \tag{19}$$

Making the overall force and energy balance along the axis of the channel allows the important flow and heat transfer properties of the friction factor f and the Nusselt number Nu to be obtained. Considering the overall force balance for the differential axial length as

$$\frac{\partial P^*}{\partial s^*} = -\frac{2f\rho w_m^{*2}}{d_H}, \qquad \frac{\partial T^*}{\partial s^*} = \frac{4q_w}{\rho c_p w_m^* d_H} \tag{20}$$

where q_w is wall heat flux and c_p is the heat capacity at constant pressure. Combining the above equations into a dimensionless form while considering the definition of Nusselt number, we can obtained

$$f = -\frac{1}{2Re^2}\frac{\partial P}{\partial s}, \qquad Nu = \frac{Re}{4T_b} \tag{21}$$

where T_b is the dimensionless bulk mean temperature.

3. Numerical method of solution

The governing equations (10)–(14) are a set of convection-diffusion equations with velocity-pressure coupling. In order to obtain solutions for these kinds of equations, we chose the finite-volume method. The power-law scheme was used to discretize the convection term and the SIMPLE scheme was employed to deal with the problem of velocity-pressure coupling. The mesh system was staggered and an alternating direction line by line iterative method (ADI) with block correction technique was used to solve the discretization equations. The description of the numerical implementation can be found in Patankar [24].

For a given Dn, an iterative procedure should be applied to obtain a specific value of axial pressure gradient $-\partial P/\partial s$. A value of $-\partial P/\partial s$ was first guessed and the flow rate thusly obtained was compared with the given flow rate. If the former was smaller (or larger) than the latter, we would increase (or decrease) $-\partial P/\partial s$ until the two flow rates almost reach a same value. The convergence criterion was $|(\phi^{n+1} - \phi^n)/\phi^n| < 10^{-7}$.

To check the grid dependence, we examined three pairs of grid sizes in the flow domain. Table 2 gives variations of the friction factor ratio f/f_s, the dimensionless maximum axial velocity $w_{\max}$ and the Nusselt number ratio Nu/Nu_s with different grids. We can see that there is almost less than 1% difference for f/f_s, $w_{\max}$ and Nu/Nu_s between the grid system 42×42 and 62×62. To save CPU time, we adopted the grid system 42×42 in this problem.

In order to examine the accuracy of the calculation code, we examined the flow in the stationary toroidal and helical square ducts ($F = 0$). The friction factor ratios of f/f_s obtained in the present analysis are shown with previous results in Fig. 2. The numerical procedure is used with a symmetrical boundary and

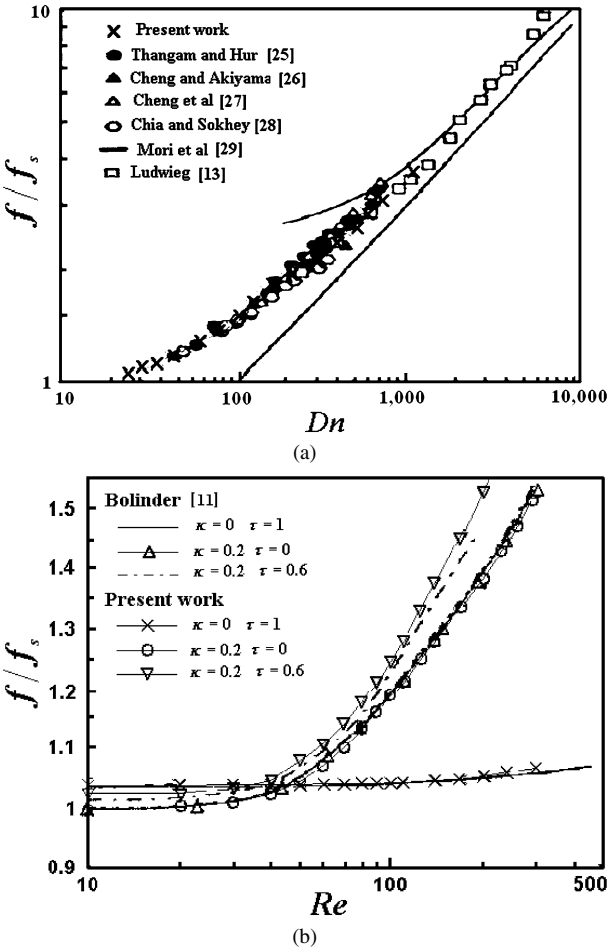

Fig. 2. Comparison of f/f_s with available result: (a) $\tau = 0$, $F = 0$; (b) $F = 0$.

Table 1
The comparison of Nu with available results ($\kappa = 0.1$, $\tau = 0.0$, $Pr = 10$)

Dn	Nu		
	Present results	Thomson et al. [12]	% difference
5	3.65	3.66	0.27
20	5.64	5.67	0.53
35	8.05	8.11	0.74

Table 2
Variation of f/f_s, $w_{\max}$ and Nu/Nu_s with different grids ($Dn = 50$, $\kappa = 0.2$, $\tau = 0.2$, $Pr = 0.71$)

F	Grid	f/f_s	$w_{\max}$	Nu/Nu_s
0	22×22	1.2793	1.8055	1.3491
	42×42	1.2216	1.8818	1.3013
	62×62	1.2216	1.8922	1.2947
20	22×22	2.5686	1.3828	1.6622
	42×42	2.4755	1.4350	1.5902
	62×62	2.4613	1.4436	1.5814
−20	22×22	2.4532	1.4133	1.6265
	42×42	2.3879	1.4824	1.5731
	62×62	2.3705	1.4899	1.5690

the curvature for this case is small, such as $\kappa = 0.01$. Fig. 2 shows that the present results are in good agreements with the previous results. Table 1 shows the comparison of the Nusselt number with previous results ($\kappa = 0.1$, $\tau = 0.0$). It can also be found that the computed Nusselt number agrees very well with the published data.

4. Results and discussions

A remarkable property of the flow in a rotating helical square duct is the coexistence of rotation, curvature and torsion, which makes the flow and heat transfer behaviors very complex. Because F represents the ratio of the Coriolis force to the centrifugal force and denotes the degree of the effect of torsion, we will change F and τ continuously to check the combined effects of rotation and torsion on the flow behaviors, temperature distribution, friction factor, and Nusselt number. In the contour diagrams, solid, dotted and dot-dash lines indicate positive, zero and negative values respectively. The outer bend side is on the left for all of the flow structure and temperature figures.

4.1. Variation of flow behaviors and distributions of temperature with rotation

Firstly, we checked the effects of rotation on the flow behaviors and the distributions of temperature. Fig. 3(a)–(f) shows the flow behavior and distribution of temperature at various values of F. The figures show the view from the upstream of the duct. Viewing from left to right the figures are the vector plots of secondary flow, the contours of stream function, the equivelocity lines of the axial velocity, and the isotherms. In the contour diagrams of stream function, axial velocity and temperature, the increment is 0.5, 0.2 and 1, respectively. According to Eq. (15), the stream function in helical ducts does not define streamlines for the secondary flow. It includes the secondary flow and the convective transport by the axial flow and it is useful if one wants to explain the convective transport of heat and momentum, see Eq. (16). In this paper we present the contours of stream function to understand convection of fluid particles in the cross-section of the duct and we present the secondary velocity vector plots to understand the secondary flow structure. The former can be illustrated by the traces of smoke in a visualization photograph taken at a cross-section, and the later can be measurable experimentally by a pointing device.

As shown in Fig. 3(c) at $F = 0$, a pair of vortices with unequal size is located at the vector plot of secondary flow. The vortex rotating in the same direction of torsion is larger and locates at the lower half of the cross-section. On the other hand, the vortex rotating in the opposite direction of torsion is a little smaller. But in the contour of stream function, it is seen that the higher negative ψ vortex is larger than the lower positive vortex. This figure also shows the location of the maximum axial being at the left upper part of the cross-section. Here, the distribution of temperature is similar to that of axial velocity. Next we increase F to the point, where $F = 2$, to check the effects of co-rotation (see Fig. 3(b)). For $F = 2$, the Coriolis force is in the same direction as the centrifugal force. There is no qualitative difference in the vector plot of secondary flow between $F = 2$ and $F = 0$, but in the contours of the stream function, the upper negative vortex has almost the same size as the lower positive vortex whereas the intensity of two vortices become stronger. Here, the effects of increasing F are similar to that of increasing the Dean number.

To check the flow behaviors and distribution of temperature in a high rotating speed, we increase F to the point where $F = 30$. It is seen that the Taylor–Proudman effect appears. Here the contour of axial velocity shows a dumbbell structure and the axial iso-velocity lines are almost constant in the rotational vector direction in the inviscid core of the flow, whereas the secondary streamlines are almost symmetrical up and down. Let us make some explanations on this phenomenon. the Coriolis force and the centrifugal force affect the axial velocity through the net force (from Eq. (13))

$$f_r = 2\kappa wu/M + 2u\kappa F \tag{22}$$

For a positive F, near horizontal line, $u < 0$, the above expression is negative and will decrease the local axial velocity, whereas near the upper and lower wall, $u > 0$ which will increase the axial velocity near the wall. When F is small, this effects can be neglected because the above expression is very small, but as F becomes large, the above expression becomes lager and larger, at last, it results in a dumbbell like shape of the axial velocity contours with two high regions near the upper and lower wall. At this moment, there exists an evident difference between the distribution of temperature and that of axial velocity. And the maximum temperature is near the center of the cross-section.

We next discuss the effects of counter-rotation on the flow behaviors and distribution of temperature. Now we decrease F to the point where $F = -1.3$. At this point, the Coriolis force and the centrifugal force have almost comparable order

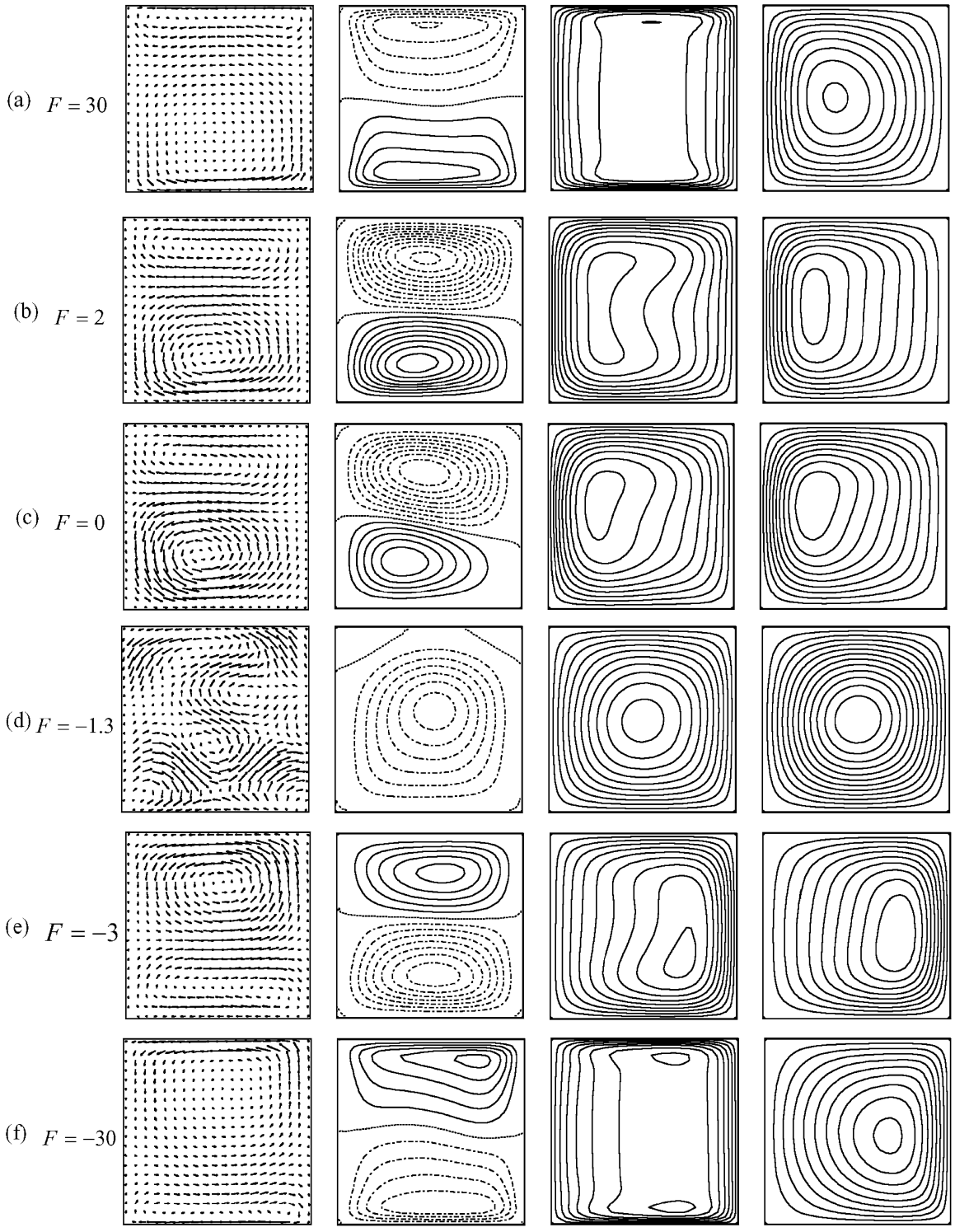

Fig. 3. The variation of flow patterns and temperature distributions with F ($\tau = 0.2$, $\kappa = 0.2$, $Dn = 50$, and $Pr = 0.71$).

of magnitude but in the opposite direction. As seen in Fig. 3(d), the flow behaviors show some interesting features. Here, the flow behaviors are similar to those in a straight twist duct, the two previous vortices become an almost single negative ψ vortex. The maximums of axial velocity and temperature move to the center of the cross-section. This phenomenon indicates that when the Coriolis force and the centrifugal force almost counteract each other, the torsion factors cause the greatest effect on the flow behaviors. If we decrease F further, where $F = -3$, the inward Coriolis force dominates the flow and the flow behaviors as well as the distribution of temperature behave almost in the same way as those in the case of $F = 2$, but in reverse. When F decreases to the point, where $F = -30$, the Taylor–Proudman effects can also be found (see Fig. 3(f)), just like the figures in the co-rotation case of $F = 30$.

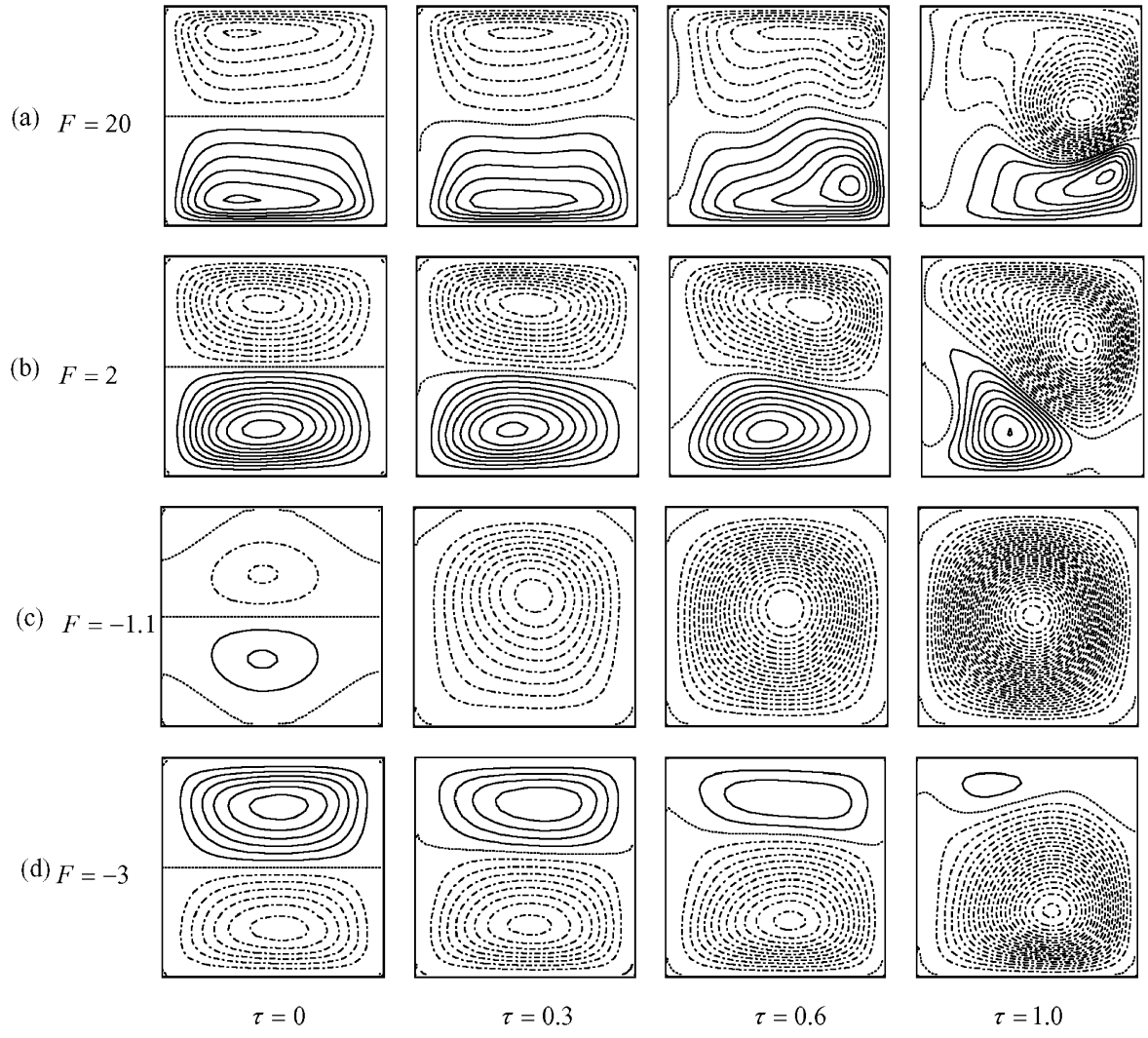

Fig. 4. Variation of constant ψ lines with τ at several F ($Dn = 50$, $\kappa = 0.2$).

4.2. Variation of flow behaviors and distributions of temperature with torsion

When torsion increases, the increasing twisting force (proportional to $\rho\tau^* w^{*2}$) will make the flow behaviors and distributions of temperature change significantly. Fig. 4 shows variation of constant ψ lines with τ for different F. The increment of ψ is 0.5. When there is no torsion, Zhang et al. [22] has made calculations. Present results without torsion show qualitative agreement with their work. When we increase τ to the point of $\tau = 0.3$, then, the symmetrical structure of contours of stream function becomes distorted. The negative ψ vortex becomes stronger as the positive ψ vortex shrinks. As τ increases, it will be seen that the negative ψ vortex becomes stronger as the positive ψ vortex shrinks gradually. As shown in Fig. 4(c), when $\tau = 1.0$, the negative vortex totally occupies the whole cross-section. Considering Eq. (6), for a sufficiently large τ, the stream function will be dominated by the torsion term. So the single negative vortex of ψ contours is expected. From Fig. 4(c) ($F = -1.1$), it is also shown that when the Coriolis force and the centrifugal force have almost comparable orders of magnitude but in the opposite direction, this phenomenon is more evident than other case.

The contours of axial velocity for various F have been examined in Fig. 5. The contour lines of the axial velocity are drawn at increments of 0.2 from the duct surface. As τ increases, the contours of the axial velocity rotate clockwise with the maximum location moving slowly to the center of the duct (seen in Fig. 5(b), (d)). In Fig. 5(d) ($F = -1.1$), it is seen that the torsion has little influence on the distribution of axial velocity. For the high speed rotating case ($F = 20$), it is seen that as τ increases, two maximum regions of axial velocity merge into one and when $\tau = 1.0$ the maximum location is almost at the center. Fig. 6 shows the temperature distributions at several values of F. We find that the effects of torsion on the temperature distribution are similar to those on the contours of axial velocity. As τ increases, the maximum temperature region rotates clockwise as the temperature maximum moves slowly to the center of the duct and when $F = -1.1$, the torsion almost has no influence on the distribution of temperature. From the phenomenon for the contours of axial velocity and temperature, we can conclude that there are only effects of the curvature or the rotation on the axial flow, the torsion effects can be recognized.

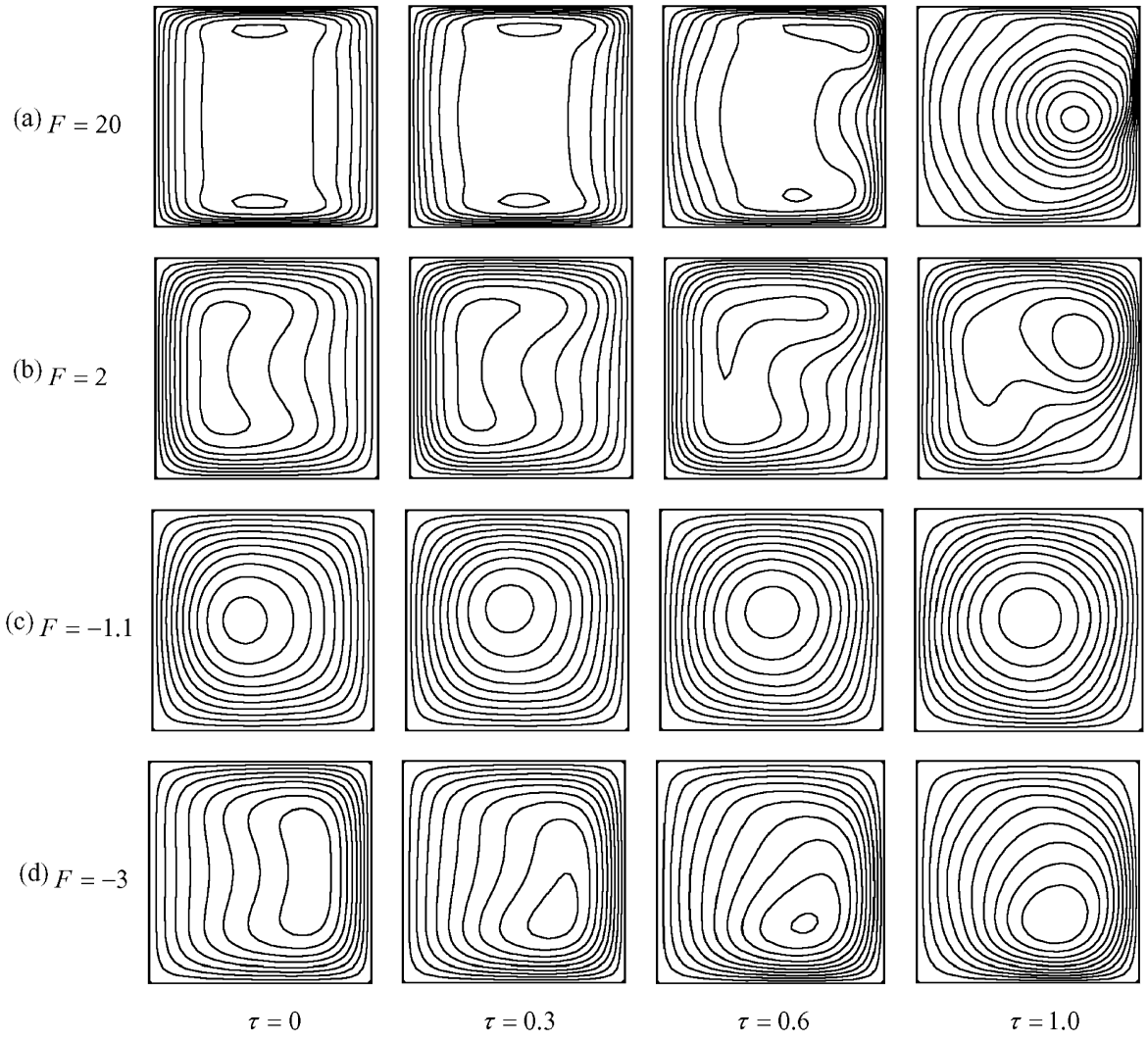

Fig. 5. Variation of axial velocity contour with τ at several F ($Dn = 50$, $\kappa = 0.2$).

4.3. Friction factor and Nusselt number

As two of the most important flow properties in engineering applications, the friction factor and the Nusselt number should be examined in detail (the expressions of friction factor and Nusselt number can be seen in Eq. (21). Fig. 7 gives the variations of the friction factor ratio f/f_s against F at $\kappa = 0.1$ and $\kappa = 0.2$. The figure shows that the friction factor ratio f/f_s reaches its minimum value of about 1.0 at the point where $F \approx -1.2$ for $\kappa = 0.1$ and $\kappa = 0.2$. This indicates that when the Coriolis force and the centrifugal force have almost comparable orders of magnitude but in the opposite direction, the friction factor in a rotating helical square ducts almost has the same value as that in a non-rotating straight square ducts. For $F < -1.2$, f/f_s decreases as F increases and for $F > -1.2$, f/f_s increases as F increases. The friction factor of $\kappa = 0.2$ is lager than that of $\kappa = 0.1$. This is well understood if we realize that ducts with high curvature make the secondary flow strong and the fluid does not flow easily. The variation of the Nusselt number ratio Nu/Nu_s with F is shown in Fig. 8. Just like the variation of the friction factor with F, when $F \approx -1.2$, the Nusselt number ratio Nu/Nu_s reaches its minimum. When $F > -1.2$, Nu/Nu_s increases as F increases from -1.2 to the point about 10 (little difference for different curvature, see Fig. 8) and then Nu/Nu_s almost keeps constant as F increases, which means that when $F > 10$, the improvement of rotating speed has almost no influence on the Nusselt number. When $F < -1.2$, Nu/Nu_s increases as F decreases from -1.2 to the point of about -10 and then almost keeps constant as F is further decreased. Fig. 8 also indicates that for a given F, the Nusselt number of $\kappa = 0.1$ is lager than that of $\kappa = 0.2$.

To study the effect of torsion on the friction factor, we examined the variation of friction factor with τ in Fig. 9. As shown in Fig. 9(a), for the co-rotation, it can be found that there exists a critical value τ_0 (τ_0 change with F), which makes f/f_s reach its maximum. When $\tau < \tau_0$, f/f_s increases as τ increases and when $\tau > \tau_0$, f/f_s decreases as τ increases. From Fig. 9(a), it is seen the larger the force ratio F is, the more evident the effects of torsion on the friction factor are. For the counter-rotation (as shown in Fig. 9(b)), the tendency of the variation of f/f_s with τ is similar to that of co-rotation, when $F = -1.2$, the torsion almost has no influence on the friction factor and f/f_s almost keeps constant as τ is increased.

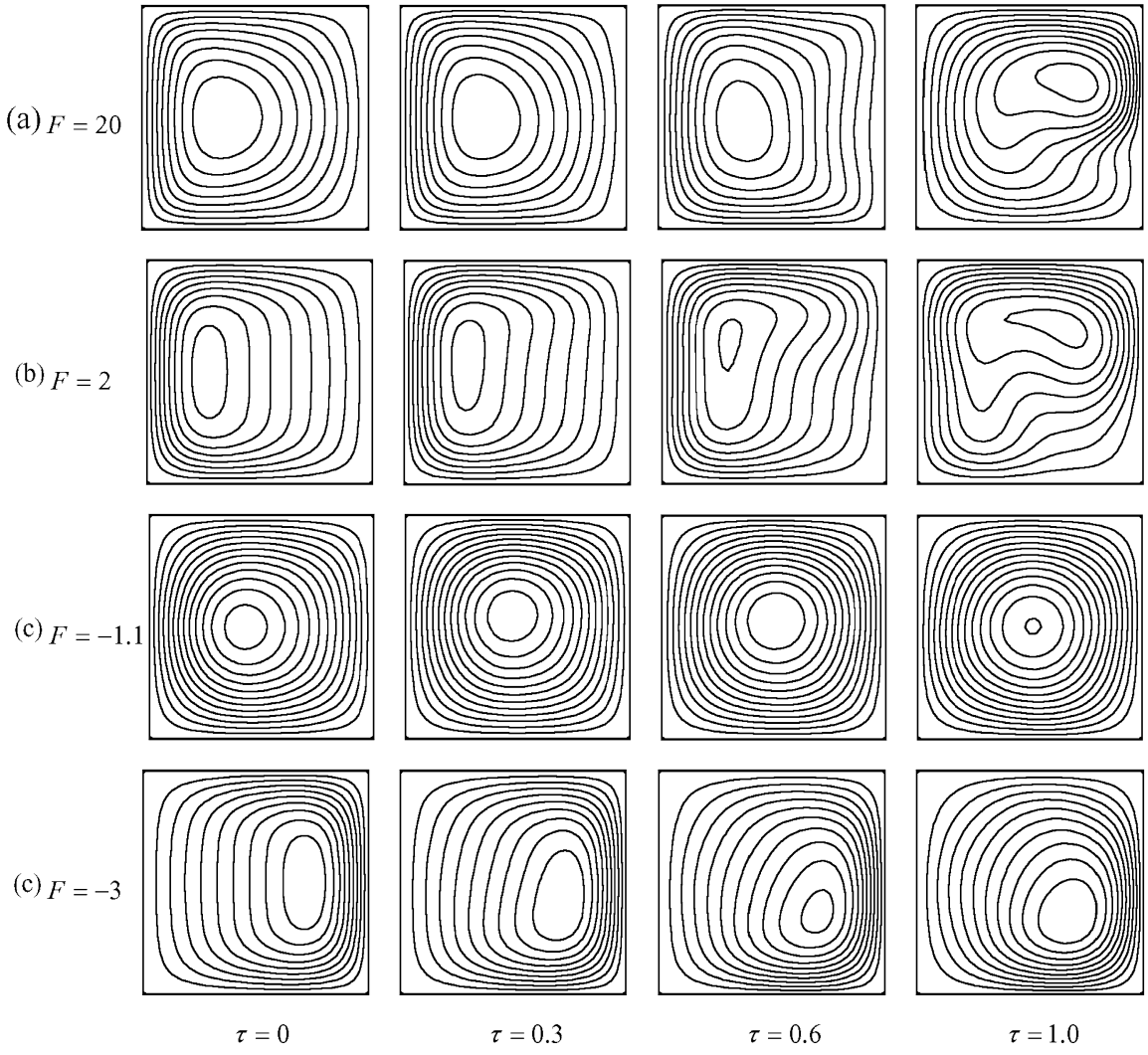

Fig. 6. Variation of distribution of temperature with τ at several F ($Dn = 50$, $Pr = 0.71$).

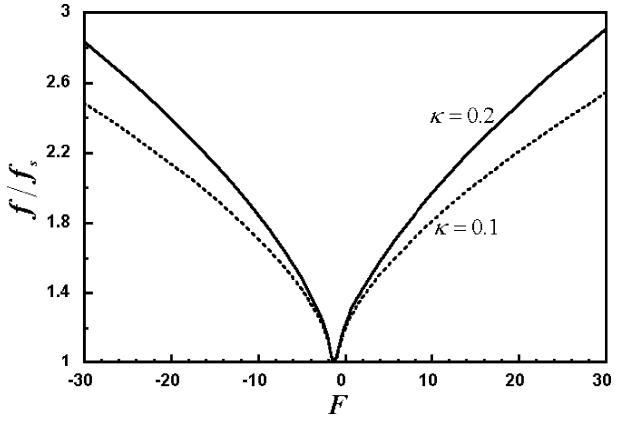

Fig. 7. Variation of friction factor ratio for different values of κ with F ($Dn = 50$ and $\tau = 0.2$).

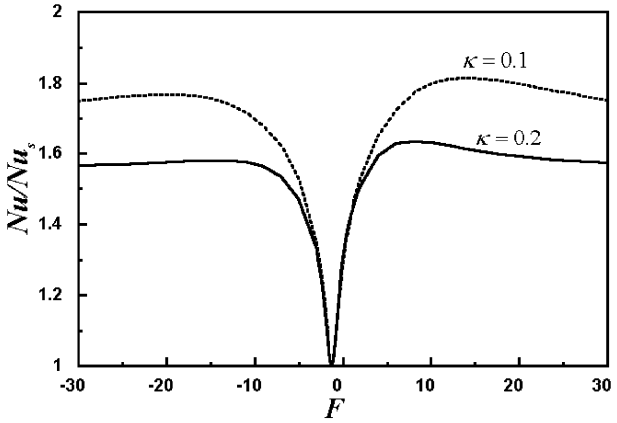

Fig. 8. Variation of Nusselt number ratio for different values of κ with F ($Dn = 50$, $\tau = 0.2$, $Pr = 0.71$).

As was pointed out before, torsion will cause a decrease in the Nusselt number compared to pure toroidal flow for the stationary cases (Thomson et al. [12]). To examine the effect of torsion on the flow in a rotating helical square duct, we present the variation of Nu/Nu_s with τ at several values of F in Fig. 10. For the stationary case ($F = 0$), the results show good agreement with Thomson et al. [12]. However, when rotation exists, as indicated in the figure, this conclusion for the stationary helical square ducts does not hold true. For the co-rotation $F > 0$ (as seen in Fig. 10(a)), it can be found that there exists a critical

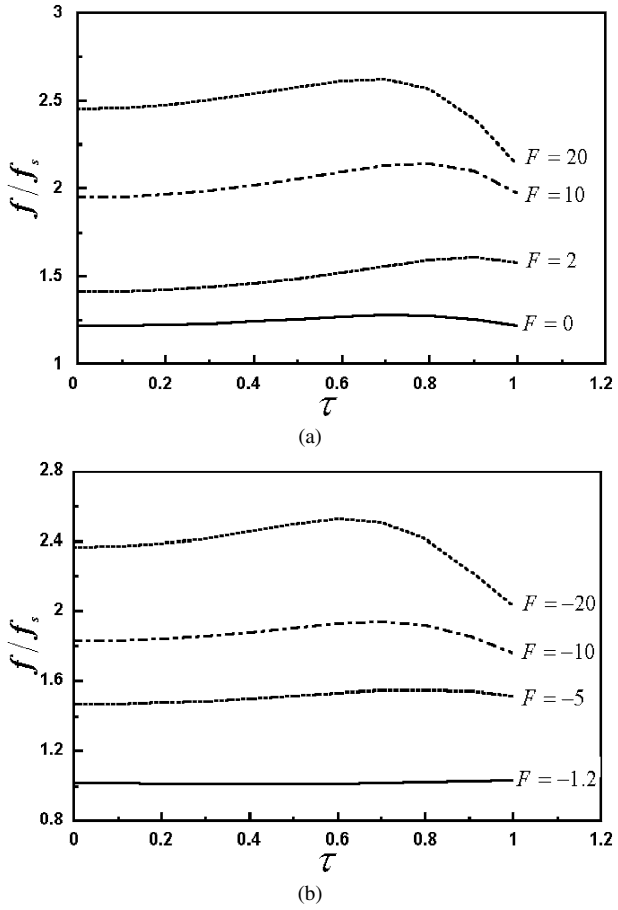

Fig. 9. Variation of friction factor ratio at several F with τ ($Dn = 50$, $\tau = 0.2$, $\kappa = 0.2$): (a) $F \geqslant 0$; (b) $F < 0$.

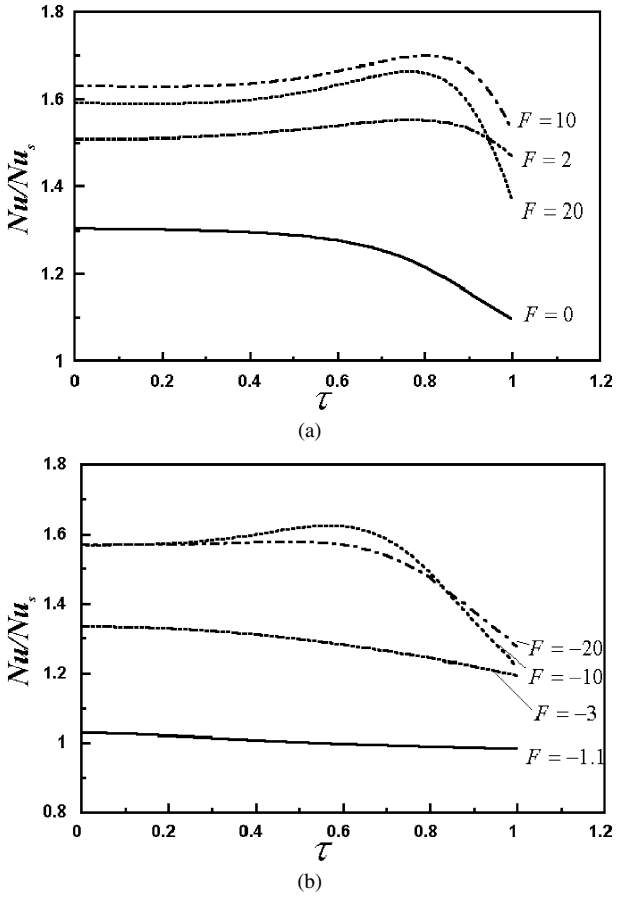

Fig. 10. Variation of Nusselt number ratio at several F with τ ($Dn = 50$, $\kappa = 0.2$, $Pr = 0.71$): (a) $F \geqslant 0$; (b) $F < 0$.

value τ_0, at where Nu/Nu_s reaches its maximum value. When $\tau < \tau_0$, Nu/Nu_s increases slowly as τ increases and then decreases as τ increases. This tendency also can be found when the rotation has the opposite direction with the axial velocity, as shown in Fig. 10(b), $F = -10$ and $F = -20$. The figure also indicates that this phenomenon will be more evident when the duct is at a high rotation speed.

4.4. Multiple solutions

When the Dean number exceeds a critical value, the curved pipe flow is known to process multiple solutions, this phenomenon is called flow bifurcation. Cheng and Akiyama [26] first found the four-cell structure of the secondary flow in a curved stationary rectangular duct. Cheng et al. [27] suggested this four-cell structure was due to the Dean-type instability or centrifugal instability and this four-cell structure has been confirmed experimentally by Cheng and Mok [30]. For the rotating toroidal pipe, the bifurcation studies can be found in Daskopoulos and Lenhoff [31] and Selmi et al. [32]. In the present study, we have also found multiple solutions for the flow in rotating toroidal pipe. However, we cannot find the multiple solutions for a helical square duct due to the existence of torsion.

In order to find the multiple solutions, two numerical procedures are used:

(I) without symmetry imposed procedure to find the unconditionally stable solution.
(II) symmetry imposed procedure to find the symmetrical stable solution.

The results for $Dn = 300$, $\kappa = 0.2$ obtained through the two procedures are shown in Fig. 11. In the figures, the stream function and axial velocity are normalized by their maximum absolute values $\psi_{\max}$, $w_{\max}$. For the case (I) (without symmetry imposed), the variation of flow structure with F is similar to that analyzed in the last section. As F decreases from a positive value to a negative value, the secondary flow due to the inward Coriolis force will appear and take over the whole cross section gradually, and also the maximum values shift from the outer wall. When $F \approx -1$, the two secondary flows can coexist on the cross-section. However, for the case (II) (symmetry imposed procedure), it will be seen that there exists an evident difference on the flow behaviors. For $F = 1$ and $F = 0$, the vortex due to the Dean-type instability appears on the cross section, we call this vortex the Dean vortex and the maximum axial velocity region is divided into two parts. As F decreases, when $F = -0.9$, the streamlines show three vortices in the upper half domain: two due to the centrifugal force and the Coriolis force and one due to flow instability (Dean vortex). As F decrease further, the secondary flow due to the Corio-

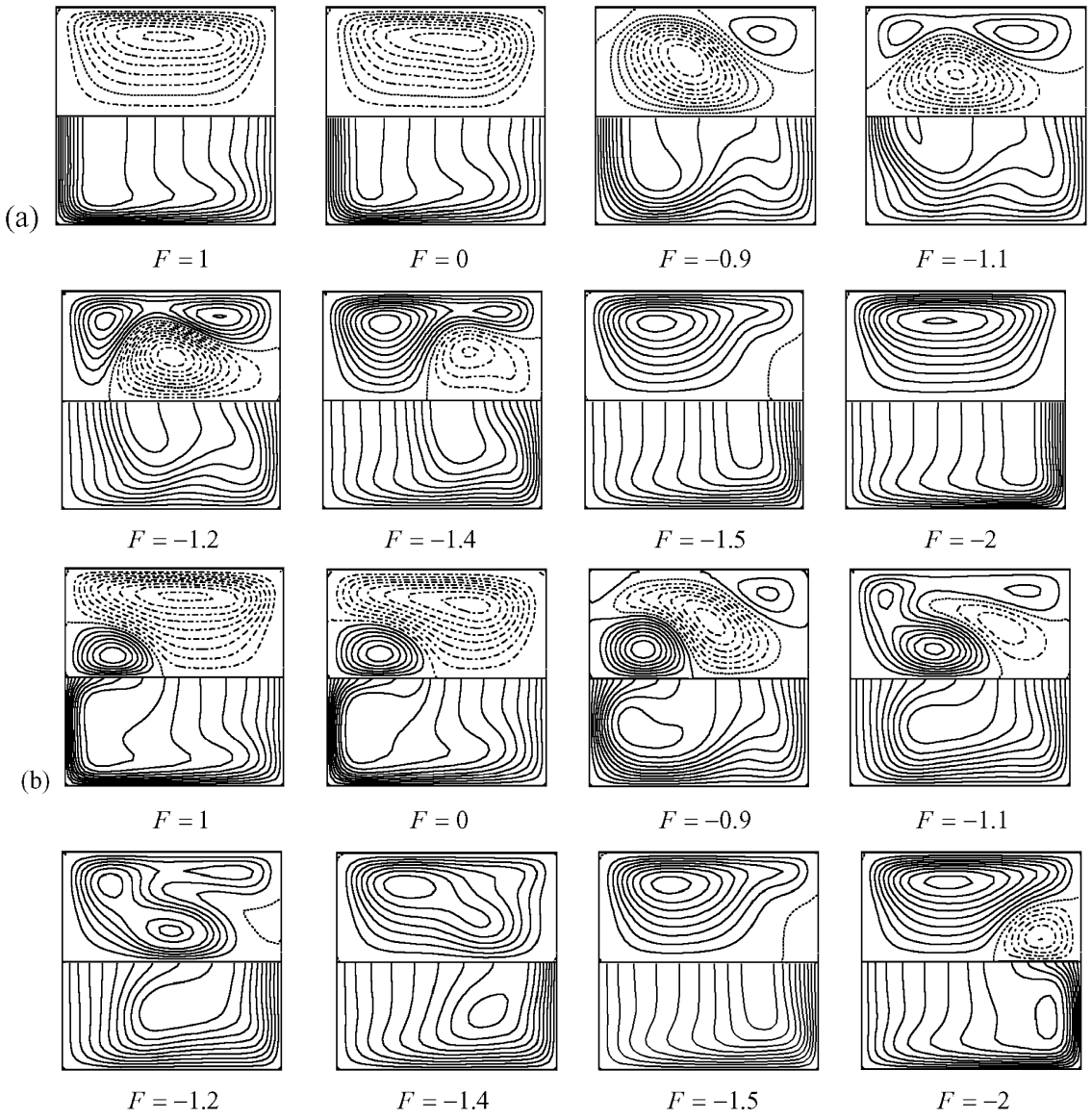

Fig. 11. Multiple solutions, (a): results from procedure (I); (b): results of procedure (II). ($Dn = 300$, $\kappa = 0.2$, $\tau = 0$, upper: secondary flow, lower: axial velocity.)

lis force and the Dean-vortex combine with each other because they have the same rotating direction, the secondary flow due to centrifugal force becomes weak and completely disappears at $F = -1.4$. As F continues to decrease, it is seen that a weak secondary flow due to centrifugal force reappears at $F = -1.5$. When $F = -2$, the Coriolis force causes a Coriolis instability near the inner wall and the vortex due to Coriolis instability, which is opposite to the Dean vortex, appears near the inner wall and the maximum location of the axial velocity is re-divided into two locations. But not liking the cases $F = 1$ and $F = 0$, these two maximum locations are near the inner wall.

5. Conclusion

In this paper, the steady fully developed fluid flow and heat transfer in a rotating helical duct with square cross section were formulated and studied numerically. The present study covers a wide range of parameters. The effects of rotation and torsion on the flow behaviors and heat transfers have been examined in details. Here are the major conclusions:

(1) Due to the rotation, there exists an obvious difference on the flow behaviors and heat transfer. For the co-rotation, the increasing rotation first appears with increasing the Dean number. And with F increasing more, the Taylor–Proundman effects appear. But for the counter-rotation, some complicated phenomena can be found. When F is about -1.20, the vector plot of secondary flow is similar to that in the straight twist ducts and only a single negative ψ vortex is observed in the cross section, causing the maximum axial velocity moves to the center of the cross-section. The reversal of flow behaviors will be seen when we proceed to decrease F. As F changes, the distribution of temperature shows a similar tendency with that of axial velocity except for the high rotating cases.

(2) As the torsion increases, the negative ψ vortex becomes stronger whereas the positive ψ vortex shrinks gradually and the maximum of the axial velocity rotates clockwise with the maximum location moving slowly to the center of the duct. The stronger the effect of rotation, the more evident the effects of torsion on flow behaviors will be.
(3) The friction factor and the Nusselt number reach their minimums value at about 1 at $F \approx -1.2$, which means, at this point, the friction factor and the Nusselt number almost have the same value as that of a stationary straight ducts. When $|F| > 10$, the improvement of rotating speed has almost no influence on the Nusselt number. As the torsion increases, both the friction factor and the Nusselt number increase, reaching a maximum and then decreasing. This tendency of variation will be more evident when the duct is in a high rotation speed.
(4) For a rotating toroidal square, we obtain the symmetrical stable solution and the unconditionally stable solution for high Dean numbers. For the counter rotation case, the Dean vortex can coexist with the vortices due to the centrifugal force and the Coriolis force at $F \approx -1$. As F decreases, the Coriolis instability will appear and the vortex due to the Coriolis instability can be generated near the inner wall.

Acknowledgements

The third author wish to thank the financial support of the National Natural Science Foundation of PR China (Grant No: 10272096).

References

[1] S.A. Berger, L. Talbot, L.S. Yao, Flow in a curved pipe, Annu. Rev. Fluid Mech. 15 (1983) 410–512.
[2] K. Nandakumar, J.H. Masiyah, Swirling flow and heat transfer in oiled and twisted pipe, Adv. Transport Processes 4 (1986) 49–112.
[3] H. Ito, Flow in curved pipe, Japan Soc. Mech. Engrg. Int. J. 30 (1987) 543–552.
[4] S.A. Berger, Flow and heat transfer in curved pipes and tubes, AIAA Paper, 1991, 91-0030.
[5] M. Germano, On the effect of torsion on a helical pipe flow, J. Fluid Mech. 125 (1982) 1–8.
[6] E.R. Tuttle, Laminar flow in twisted pipes, J. Fluid Mech. 219 (1990) 545–570.
[7] S. Liu, J.H. Masliyah, Axially invariant laminar flow in helical pipes with a finite pitch, J. Fluid Mech. 251 (1993) 315–353.
[8] L. Zabielski, A.J. Mestel, Steady flow in a helically symmetric pipe, J. Fluid Mech. 370 (1998) 297–320.
[9] W.H. Chen, R. Jan, The torsion effect on fully developed laminar flow in helical square channels, Trans. ASME J. Fluids Engrg. 98 (1993) 41–48.
[10] C.J. Bolinder, Observations and predictions of laminar flow and heat transfer in helical rectangular ducts, Doctoral thesis, Lund Institute of Technology, Sweden, 1995.
[11] C.J. Bolinder, The effects of torsion on the bifurcation structure of laminar flow in a helical square duct, Trans. ASME J. Fluid Engrg. 117 (1995) 242–248.
[12] D.L. Thomson, Y. Bayazitoglu, A.J. Meade, Low Dean number convective heat transfer in helical ducts of rectangular cross section, Trans. ASME J. Heat Transfer 120 (1998) 85–91.
[13] H. Ludwieg, Die Ausgebildete Kanalströmung in einem rotierenden System, Ingenieur-Archiv. 19 (1951) 296–308.
[14] H. Miyazaki, Combined free and force convective heat transfer and fluid flow in rotating curved circular tube, Int. J. Heat Mass Transfer 14 (1971) 1295–1309.
[15] H. Miyazaki, Combined free and forced convective heat transfer and fluid flow in a rotating curved rectangular tube, Trans. ASME C J. Heat Transfer 95 (1973) 64–71.
[16] H. Ito, T. Motai, Secondary flow in a rotating curved pipe, Rep. Inst. High Speed Mech. 29 (1974) 33–57.
[17] M.M. Menon, Periodic centrifugal separations, MS thesis, Case Western Reserve University, 1984.
[18] H. Ito, H. Aakita, S. Hasegawa, M. Suzuki, Numerical and experimental study on laminar flow in a rotating curved pipe (1. Constant Dean number), Mem. Inst. High Speed Mech. 58 (1987) 185–235.
[19] H. Ishigaki, Flow in rotating curved pipes, J. Fluid Mech. 329 (1996) 373–388.
[20] L.Q. Wang, K.C. Cheng, Flow transition and combined free and forced convective heat transfer in rotating curved channels: The case of positive rotation, Phys Fluids 8 (1996) 1153–1173.
[21] K. Yamamoto, S. Yanae, M.M. Alam, Flow through a rotating curved duct with square cross-section, J. Phys. Soc. Japan 68 (1999) 1173–1184.
[22] J.S. Zhang, B.Z. Zhang, J.W. Ju, Fluid flow in rotating curved rectangular duct, Int. J. Heat Fluid Flow 22 (2001) 583–592.
[23] B.Z. Zhang, Q. Chen, J.S. Zhang, The perturbation solutions of the flow in a curved rotating annular pipe, J. Hydrodynamic 13 (2001) 75–80.
[24] S.V. Patankar, Numerical Heat Transfer and Fluid Flow, Hemisphere, New York, 1980.
[25] S. Thangam, N. Hur, Laminar secondary flow in curved rectangular ducts, 217 (1990) 421–440.
[26] K.C. Cheng, M. Akiyama, Laminar forced convection heat transfer in curved rectangular channels, Int. J. Heat Mass Transfer 13 (1970) 471–490.
[27] K.C. Cheng, R.C. Lin, J.W. Ou, Fully developed laminar flow in curved rectangular channels, J. Fluids Engrg. 3 (1976) 41–48.
[28] K.N. Ghia, J.S. Sokhey, Laminar incompressible viscous flow in curved ducts of regular cross section, Trans. ASME J. Fluids Engrg. 99 (1977) 640–648.
[29] Y. Mori, Y. Uchida, T. Ukon, Forced convective heat transfer in a square cross section, Int. J. Heat Mass Transfer 14 (1971) 1787–1805.
[30] K.C. Cheng, S.Y. Mok, in: Fluid Control and Measurement, vol. 2, Pergamon, 1986, pp. 765–773.
[31] P. Daskopoulos, A.M. Lenhoff, Flow in curved ducts, Part 2. Rotating ducts, J. Fluid Mech. 217 (1990) 575–593.
[32] M. Selmi, K. Nandakumar, W.H. Finlay, A bifurcation study viscous flow through a rotating curved duct, J. Fluid Mech. 262 (1994) 353–375.